International Journal of Solids and Structures 80 (2016) 334–347

Contents lists available at ScienceDirect

International Journal of Solids and Structures

journal homepage: www.elsevier.com/locate/ijsolstr

Constitutive modelling of high strength titanium alloy Ti-6Al-4 V for sheet forming applications at room temperature

Ossama Mamdouh Badr[a,*], Frédéric Barlat[b], Bernard Rolfe[c], Myoung-Gyu Lee[d], Peter Hodgson[a], Matthias Weiss[a]

[a] Institute for Frontier Materials, Deakin University, Waurn Ponds, Pigdons Rd., VIC. 3217, Australia
[b] Graduate Institute for Ferrous Technology (GIFT), Pohang University of Science and Technology (POSTECH), 31 Hyoja-dong, Nam-gu, Pohang 790-784, Republic of Korea
[c] School of Engineering, Deakin University, Waurn Ponds, Pigdons Rd., VIC. 3216, Australia
[d] Department of Materials Science and Engineering, Korea University, Seoul, Republic of Korea

ARTICLE INFO

Article history:
Received 6 March 2015
Revised 24 August 2015
Available online 1 November 2015

Keywords:
Ti-6Al-4 V
Yield surface
Constitutive model
Bauschinger effect

ABSTRACT

To enable the design and optimisation of forming processes at room temperature the material behaviour of Ti-6Al-4 V needs to be accurately represented in numerical analysis and this requires an advanced material model. In particular, an accurate representation of the shape and size of the yield locus as well as its evolution during forming is important. In this study a rigorous set of experiments on the quasi-static deformation behaviour of a Ti-6Al-4 V alloy sheet sample at room temperature was conducted for various loading conditions and a constitutive material model developed. To quantify the anisotropy and asymmetry properties, tensile and compression tests were carried out for different specimen orientations. To examine the Bauschinger effect and the transient hardening behaviour in – plane tensile – compression and compression – tensile tests were performed. Balanced biaxial and plane strain tension tests were conducted to construct and validate the yield surface of the Ti-6Al-4 V alloy sheet sample at room temperature. A recently proposed anisotropic elastic-plastic constitutive material model, so-called HAH, was employed to describe the behaviour, in particular for load reversals. The HAH yield surface is composed of a stable component, which includes plastic anisotropy and is distorted by a fluctuating component. The key of the formulation is the use of a suitable yield function that reproduces the experimental observations well for the stable component. Meanwhile, the rapid evolution of the material structure must be captured at the macro - scale level by the fluctuating component embedded in the HAH model. Compared to conventional hardening equations, the proposed model leads to higher accuracy in predicting the Bauschinger effect and the transient hardening behaviour for the Ti-6Al-4 V sheet sample tested at room temperature.

1. Introduction

Because they combine high specific strength and high structural stiffness with excellent heat and corrosion resistance (Welsh et al., 1994), titanium alloys are increasingly used as structural material for aerospace (Peters et al., 2003, Moiseyev, 2005), petrochemical, marine (Gurrappa, 2003, Banker and Scaturro, 1997) and automotive (Schauerte and Ag, 2005) industries. Ti-6Al-4 V, denoted Ti64 in this article, is the most generally utilized Titanium alloy and records for more than half of the overall usage of titanium worldwide (Donachie, 2000). Since HCP-α is the dominating phase in Ti64 and the volume of dispersed BCC β-phase ($<$10%) is low at room temperature, the deformation behaviour of Ti-6Al-4 V is primarily governed by the HCP-α phase, which has only a limited number of slip systems (Donachie, 2000, Gerd Lütjering, 2007).

At room temperature HCP dominated metals are known to exhibit plastic anisotropy and a pronounced tension-compression asymmetry associated with the activation of twinning. This twinning is easily activated along the c/a axis during compression, which causes the strength differential effect (SD). However, while in commercial purity titanium (CPTi) twinning concomitantly takes place with dislocation slip at room temperature, Ti64 alloys only show mechanical twinning at high strain rates and under dynamic loading. Some studies suggest that Ti64 will only mechanically twin during deformation at room temperature if it is highly alloyed with aluminium ($>$ 5.0 wt. %) and oxygen ~0.2 wt. % (Zaefferer, 2003, Conrad, 1981, Yapici et al., 2006).

Recently, Prakash et al. (2010) demonstrated that with increasing plastic deformation (moderate strains), Ti64 exhibits a change in

* Corresponding author. Tel.: +61410086331; fax: +61352271103.
E-mail address: o.badr@deakin.edu.au, metbadr79@hotmail.com (O.M. Badr).

http://dx.doi.org/10.1016/j.ijsolstr.2015.08.025
0020-7683/

texture and Lowden and Hutchinson (1975) referred this asymmetry to the differences in the hydrostatic stress level along the c- axis of the texture between tension and compression. This leads to the asymmetry of dislocation motion between the usual slip $\langle 11\bar{2}0\rangle$ and the $\langle c+a\rangle$ cross slip $\langle 11\bar{2}3\rangle$ which affects the potential for texture strengthening, and results in different texture evolutions. To accurately describe the plastic deformation of Ti64, it is important to account for those deformation mechanisms and the resulting hardening behaviour difference in tension and compression. However due to the lack of suitable macroscopic constitutive models, the classical anisotropic yield function formulated by Hill (1948), accompanied with the conventional isotropic hardening approach, is still applied to represent the behaviour of Ti64 in sheet forming simulations (Djavanroodi and Derogar, 2010). To the authors' knowledge, the development of a constitutive model capable of precisely describing the behaviour of Ti64 during load reversal has not been attempted yet. The vast majority of the previous studies focused on other HCP metals rather than Ti64 alloy sheet as extensively reviewed in (Banabic et al., 2010).

Recently, Cazacu et al., (2006) developed an anisotropic-asymmetric yield criterion, the so-called CPB06, to account for the anisotropy and the SD effect associated with twinning for pressure insensitive materials. It was reported that CPB06 is highly accurate in reproducing the yield surfaces of magnesium and CPTi (Cazacu et al., 2006). Khan et al. (2007) also applied this criterion to predict the yield locus of Ti64 and its asymmetry in yielding but reported a low level of accuracy (Khan et al., 2007). Plunkett et al. 2008 improved the capability of the CPB06 model to represent yield surface asymmetry by introducing additional linear transformation tensors operating on the Cauchy stress deviator; Namely, two linear transformations were performed for CPB06ex2 and three for CPB06ex3 (Plunkett et al., 2006). In a later study, Gilles et al. (2011) applied the orthotropic asymmetry yield criteria CPB06, CPB06ex2 and CPB06ex3 in combination with a hardening model developed by Plunkett et al. (2006), which accounts for distortional hardening due to texture evolution. With regard to describing the in-plane anisotropy of the sheet, a lower accuracy was achieved for CPB06 compared to the other two yield functions CPB06ex2 and CPB06ex3. Additionally, these yield functions led to significant differences with measured yield surfaces for Ti64 in biaxial and plane stress conditions. The authors further suggested that for an accurate description of the yield surface evolution with accumulated plastic strain, additional hardening parameters would be required. In other words, to date, there is no constitutive model allowing an accurate representation of plastic anisotropy and hardening for Ti64 at room temperature, especially if the metal strip undergoes non-monotonic deformation. To enable the widespread application of Ti64, advanced constitutive material models for the prediction of the inelastic behaviour of the material under different stress states, stress reversals and other non-proportional loading cases need to be developed (Chung and Shah, 1992).

The present paper aims at developing a novel constitutive model that is capable of representing the mechanical response of Ti64 at room temperature during load reversal. According to the literature, the asymmetry, e.g., tension-compression, in the room temperature deformation behaviour of Ti64 is insignificant at moderate strain levels and this is in contrast to CPTi in which, the asymmetry has been shown to initiate from the onset of yielding (Nixon et al., 2010, Salem et al., 2003). In Section 5 of this article, the actual yield locus of Ti64 is first experimentally determined while, in Section 6, a proposed constitutive material model is developed. Here the distortional hardening of Ti64 under multiple or continuous load changes is accounted for using the homogenous anisotropic hardening model, the so called HAH approach, proposed recently by Barlat et al. (2011). In this model, the yield surface that corresponds to the stable component of the HAH model expands around the active stress state identically to that of the isotropic hardening model for the case of monotonic loading. However, the shape of the yield surface is highly distorted away from the active stress state. During a subsequent reverse loading, the new yield stress is strongly affected by the distorted yield surface, which recovers its original shape progressively near the new stress state unless permanent softening is considered. In this manner, the asymmetry in hardening behaviour resulting from the Bauschinger effect is taken into account. This approach was recently implemented into the commercial software Abaqus implicit through the user subroutine UMAT and the FE- code formulation shown in Section 2.2. The comparison with experiments for cyclic hardening of Ti64, under different loading directions validated the model which allowed capturing the main characteristics of one deformation cycle of Ti64 in the tension compression test.

2. Elastic–plastic model of Ti-64 alloy sheet at room temperature

2.1. Theoretical framework

Recently Barlat et al. (2011) proposed the HAH model, a homogenous yield function Φ based anisotropic hardening model. The model accounts for asymmetric yielding resulting from loading path changes and pre-deformation. A brief over view of this model is given below; a description in detail can be found in (Barlat et al., 2011). The criterion is expressed as a combination of a stable component φ and the fluctuating component φ_h:

$$\Phi(\mathbf{s}) = [\varphi^q + \varphi_h^q]^{\frac{1}{q}} = \Big[\varphi^q + |f_1\,\hat{\mathbf{h}}^s:\mathbf{s} + f'_1|\hat{\mathbf{h}}^s:\mathbf{s}||^q + |f_2\hat{\mathbf{h}}^{\mathbf{s}}:\mathbf{s} - \mathbf{f'_2}|\hat{\mathbf{h}}^{\mathbf{s}}:\mathbf{s}||^{\mathbf{q}}\Big]^{\frac{1}{q}} = \bar{\sigma}(\boldsymbol{\sigma}) \tag{1}$$

Any regular isotropic or anisotropic homogenous yield function of first order in the form of $\Phi(\mathbf{s}) = \bar{\sigma}(\boldsymbol{\sigma})$ can be used as a stable component with the effective stress $\bar{\sigma}$. The distortion of the yield locus resulting from the loading history and the corresponding asymmetric hardening is introduced by φ_h while the exponent q controls the shape of the yield surface. The parameter φ_h depends on the stress deviator $\mathbf{s}$, the microstructure deviator $\hat{\mathbf{h}}^s$, and state variables with a particular assumption of $f_1 = f'_1$ and $f_2 = f'_2$. In Eq. (1) the microstructure deviator, $\hat{\mathbf{h}}^s$ is introduced to capture and memorize the previous deformation history. It is defined as the normalized tensor of the traceless deviator $\mathbf{h}^s$ given in Eq. (2). The constant 8/3 is introduced in Eq. (2) as a matter of convenience to describe the microstructure history deviator in a similar manner to the normalized strain rate tensor before and after the strain path change as explained in detail by Barlat et al. (2011).

$$\widehat{\mathbf{h}}^s = \frac{\mathbf{h}^s}{\sqrt{\frac{8}{3}\,\mathbf{h}^s:\,\mathbf{h}^s}} \tag{2}$$

For the undeformed case $\mathbf{h}^s$ is equal to the stress deviator $\mathbf{s}$ (both are having the same unit, MPa) and remains constant as long as the loading path keeps unchanged. Once the loading direction is changed so that $\mathbf{h}^s \neq \mathbf{s}$, $\hat{\mathbf{h}}^s$ evolves as:

$$\frac{d\hat{\mathbf{h}}^s}{d\bar{\varepsilon}} = \begin{Bmatrix} k\Big[\hat{\boldsymbol{s}} - \frac{8}{3}\hat{\mathbf{h}}^s\Big(\hat{\boldsymbol{s}}:\hat{\mathbf{h}}^s\Big)\Big] \Rightarrow \hat{\boldsymbol{s}}:\hat{\mathbf{h}}^s \geq 0 \\ k\Big[-\hat{\boldsymbol{s}} + \frac{8}{3}\hat{\mathbf{h}}^s\Big(\hat{\boldsymbol{s}}:\hat{\mathbf{h}}^s\Big)\Big] \Rightarrow \hat{\boldsymbol{s}}:\hat{\mathbf{h}}^s < 0 \end{Bmatrix} \tag{3}$$

where $\hat{\boldsymbol{s}}$ is equivalent to $\mathbf{s}$ but normalized in the form of Eq. (2). With the new loading path $\hat{\mathbf{h}}^s$ rotates from its previous straining state towards $\hat{\boldsymbol{s}}$ by Eq. (3) at a rate controlled by k.The two variables f_1 and f_2 in Eq. (1) are functions of the two state variables g_1 and g_2, and can be expressed as

$$f_x = \left[g_x^{-q} - 1\right]^{\frac{1}{q}} \Rightarrow for\ x = 1:2 \tag{4}$$

where g_x physically represents the approximate ratio of the current flow stress to that of the hypothetical isotropic hardening flow stress,

i.e., $\boldsymbol{\sigma} = g_x \boldsymbol{\sigma}_{iso}$, where $x = 1$ or 2 depending on the sign of $\hat{\boldsymbol{s}} : \hat{\mathbf{h}}^s$. As soon as the material is plastically strained the state variables g_1 and g_2 evolve following the differential system below

$$\frac{dg_1}{d\bar{\varepsilon}} = \begin{Bmatrix} k_2\left(k_3\dfrac{H(0)}{H(\bar{\varepsilon})} - g_1\right) & \Rightarrow \hat{\boldsymbol{s}} : \hat{\mathbf{h}}^s \geq 0 \\ k_1\dfrac{g_4 - g_1}{g_1} & \Rightarrow \hat{\boldsymbol{s}} : \hat{\mathbf{h}}^s < 0 \end{Bmatrix} \tag{5}$$

$$\frac{dg_2}{d\bar{\varepsilon}} = \begin{Bmatrix} k_1\dfrac{g_3 - g_2}{g_2} & \Rightarrow \hat{\boldsymbol{s}} : \hat{\mathbf{h}}^s \geq 0 \\ k_2\left(k_3\dfrac{H(0)}{H(\bar{\varepsilon})} - g_2\right) & \Rightarrow \hat{\boldsymbol{s}} : \hat{\mathbf{h}}^s < 0 \end{Bmatrix} \tag{6}$$

$$\frac{dg_3}{d\bar{\varepsilon}} = \begin{Bmatrix} 0 & \Rightarrow \hat{\boldsymbol{s}} : \hat{\mathbf{h}}^s \geq 0 \\ k_5(k_4 - g_3) & \Rightarrow \hat{\boldsymbol{s}} : \hat{\mathbf{h}}^s < 0 \end{Bmatrix} \tag{7}$$

$$\frac{dg_4}{d\bar{\varepsilon}} = \begin{Bmatrix} k_5(k_4 - g_4) & \Rightarrow \hat{\boldsymbol{s}} : \hat{\mathbf{h}}^s \geq 0 \\ 0 & \Rightarrow \hat{\boldsymbol{s}} : \hat{\mathbf{h}}^s < 0 \end{Bmatrix} \tag{8}$$

where the coefficients k_1, k_2 and k_3 are associated to the evolution of g_1 and g_2, and control the reloading flow stress and transient hardening. The additional state variables g_3 and g_4 characterize the permanent softening that the material may experience upon reverse loading. If the material does not exhibit any permanent softening the model is simplified to $g_3 = g_4 = 1$ and $k_4 = 1$ or $k_5 = 0$ .While $H(\bar{\varepsilon})$ is the classical isotropic hardening curve and k_1–k_5 are material coefficients. In order to describe the material behaviour under a condition of loading change, the material coefficients k_1–k_5 have to determine by performing several sets of experiments recommended in (Barlat et al., 2011).

2.2. Formulation of FE code

The HAH model was previously implemented into the FE code Abaqus by Lee et al. (2012) and the same approach is followed here in conjunction with the yield function of Ti64 determined in this study. According to the incremental deformation theory (Chung and Richmond, 1993) the strain increments are assumed to be expressed by the discrete true strain increment, i.e. $d\boldsymbol{\varepsilon} = \Delta\boldsymbol{\varepsilon}, d\boldsymbol{\varepsilon}^e = \Delta\boldsymbol{\varepsilon}^e, d\boldsymbol{\varepsilon}^p = \Delta\boldsymbol{\varepsilon}^p, d\bar{\varepsilon} = \Delta\bar{\varepsilon}$. Where the superscripts e and p stand for the elastic and the plastic components of true strain. The total strain is decomposed into the elastic $\Delta\varepsilon^e$ and the plastic $\Delta\varepsilon^p$ components, and the linear elasticity laws applied are given below

$$\Delta\boldsymbol{\varepsilon}^p = \Delta\boldsymbol{\varepsilon} - \Delta\boldsymbol{\varepsilon}^e \tag{9}$$

$$\Delta\boldsymbol{\sigma} = \mathbf{C}.\Delta\boldsymbol{\varepsilon}^{\boldsymbol{e}} = \mathbf{C}.\Delta\boldsymbol{\varepsilon} - \mathbf{C}.\Delta\boldsymbol{\varepsilon}^p \tag{10}$$

where $\mathbf{C}$ is the elastic stiffness matrix. The equivalent plastic strain increment $\Delta\bar{\varepsilon}$ for a given $\Delta\varepsilon$ can be determined using the nature of a first degree homogeneous function $\bar{\sigma}(\boldsymbol{\sigma}) = \boldsymbol{\sigma} : \frac{\partial\bar{\sigma}}{\partial\boldsymbol{\sigma}}$ with the associated flow rule

$$\Delta\bar{\varepsilon} = \frac{\boldsymbol{\sigma}.\Delta\boldsymbol{\varepsilon}^p}{\bar{\sigma}(\boldsymbol{\sigma})} = \frac{\boldsymbol{\sigma}.\Delta\lambda\frac{\partial\bar{\sigma}}{\partial\boldsymbol{\sigma}}}{\bar{\sigma}(\boldsymbol{\sigma})} = \Delta\lambda\frac{\bar{\sigma}(\boldsymbol{\sigma})}{\bar{\sigma}(\boldsymbol{\sigma})} = \Delta\lambda \tag{11}$$

$$\Delta\boldsymbol{\varepsilon}^p = \Delta\lambda\frac{\partial\bar{\sigma}}{\partial\boldsymbol{\sigma}} = \Delta\bar{\varepsilon}\frac{\partial\bar{\sigma}}{\partial\boldsymbol{\sigma}} \tag{12}$$

where $\Delta\lambda$ is the plastic multiplier. The increments of the other state variables in the HAH model $g_1 \rightarrow g_4$ and microstructure deviator $\Delta\hat{\mathbf{h}}^s$ are expressed as functions of $\Delta\bar{\varepsilon}$ (equivalent plastic strain increment) by the discrete incremental forms of Eqs. (2)–(8). They are updated when $\Delta\bar{\varepsilon}$ is obtained during the stress integration procedure i.e. $\Delta\bar{\varepsilon}$ is the only unknown. In order to determine $\Delta\bar{\varepsilon}$ and update the stress algorithm the general convex cutting plane method (GCPM) is applied in this FE formulation. The advantage of this method is that bypasses the need for computing the gradients of the flow and the hardening law by simply obtaining $\Delta\bar{\varepsilon}$ from the consistency condition which is expressed as (Simof and Hughes, 2008)

$$\Psi = \left[\varphi^q + \varphi_h^q\right]^{\frac{1}{q}} - H(\bar{\varepsilon}) = 0 \tag{13}$$

Hence the condition for plastic yielding can be expanded in terms of the incremental change as

$$\Psi = \bar{\sigma}\left(\boldsymbol{\sigma}_i + \Delta\boldsymbol{\sigma}, f_{1,i} + \Delta f_{1,i}, f_{2,i} + \Delta f_{2,i}, \hat{\mathbf{h}}_i^s + \Delta\hat{\mathbf{h}}^s\right) - H(\bar{\varepsilon}_i + \Delta\bar{\varepsilon}) = 0 \tag{14}$$

where the subscript i refers to the initial (known) value from the previous time step. By applying Taylor's expansion, the consistency condition $\Delta\Psi = 0$ gives the expression (Lee et al., 2012)

$$\Psi + \Delta\Psi = \Psi + \frac{\partial\Psi}{\partial\Delta\bar{\varepsilon}}\delta(\Delta\bar{\varepsilon}) = 0 \tag{15}$$

which leads to,

$$\delta(\Delta\bar{\varepsilon}) = -\frac{\Psi}{\partial\Psi/\partial\Delta\bar{\varepsilon}} \tag{16}$$

From Eq. (14)

$$\frac{\partial\Psi}{\partial\Delta\bar{\varepsilon}} = \frac{\partial\Psi}{\partial\boldsymbol{\sigma}}\frac{\partial\boldsymbol{\sigma}}{\partial\Delta\bar{\varepsilon}} + \frac{\partial\Psi}{\partial H}\frac{\partial H}{\partial\Delta\bar{\varepsilon}} \tag{17}$$

where

$$\frac{\partial\Psi}{\partial\boldsymbol{\sigma}} = \frac{\partial\bar{\sigma}}{\partial\boldsymbol{\sigma}}; \quad \frac{\partial\Psi}{\partial H} = -1 \tag{18}$$

Therefore,

$$\frac{\partial\Psi}{\partial\Delta\bar{\varepsilon}} = -\mathbf{C}\frac{\partial\bar{\sigma}}{\partial\boldsymbol{\sigma}} \tag{19}$$

By substituting Eqs. (17)–(19) in Eq. (16) the following estimate of $\delta(\Delta\bar{\varepsilon})$ is obtained

$$\delta(\Delta\bar{\varepsilon}) = \frac{\Psi}{\frac{\partial\bar{\sigma}}{\partial\boldsymbol{\sigma}}\mathbf{C}\frac{\partial\bar{\sigma}}{\partial\boldsymbol{\sigma}} + H'(\bar{\varepsilon})} \tag{20}$$

where $H'(\bar{\varepsilon}) = \frac{\partial H(\bar{\varepsilon})}{\partial\bar{\varepsilon}}$ is the partial derivative of flow hardening in regard to the equivalent plastic strain $\bar{\varepsilon}$ which represents the slope of the monotonic flow curve (Lee et al., 2012) . In this way the unknown value of $\Delta\bar{\varepsilon}$ that fulfils Eq. (14) can be determined by an iterative algorithm based on the predictor – corrector scheme with the Newton–Raphson method. For a given total strain increment $\Delta\varepsilon_{n+1}$ at the current time step $t+1$ the trial stress is assumed to be pure elastic using Eq. (10) and can be calculated with

$$\boldsymbol{\sigma}_{t+1}^{(tr)} = \boldsymbol{\sigma}_t + \mathbf{C}\Delta\boldsymbol{\varepsilon}_{t+1} \tag{21}$$

where the superscript tr denotes the trial state and the subscripts t and $t+1$ correspond to the previous and the current step time, respectively. If the check for the following condition Eq. (22) is satisfied, then the trial state is accommodated to be elastic without further iteration over the time step $[t,\ t+1]$. The algorithm then moves to the next time step by updating the stress with the same value of the trial stress $\boldsymbol{\sigma}_{t+1}^{(tr)}$whilst the other state variables remain unchanged.

$$\Psi\left(\boldsymbol{\sigma}_{t+1}^{(tr)}\right) = \left[\varphi^q\left(\boldsymbol{\sigma}_{t+1}^{(tr)}\right) + \varphi_h^q\left(\boldsymbol{\sigma}_{t+1}^{(tr)}\right)\right]^{\frac{1}{q}} - H(\bar{\varepsilon}_t) \leq 0 \tag{22}$$

If the condition in Eq. (22) is not satisfied or $\Psi(\boldsymbol{\sigma}_{t+1}^{(tr)}) > 0$ the stress trial at the current time step is a plastic state and the predictor-corrector iterative algorithm commences the trial stress state as an initial estimate. The $\Delta\bar{\varepsilon}$ is then is updated for the (m)th iteration with

$$(\Delta\bar{\varepsilon}_{t+1})^{(m+1)} = (\Delta\bar{\varepsilon}_{t+1})^{(m)} + \delta(\Delta\bar{\varepsilon}_{t+1})^{(m)} \tag{23}$$

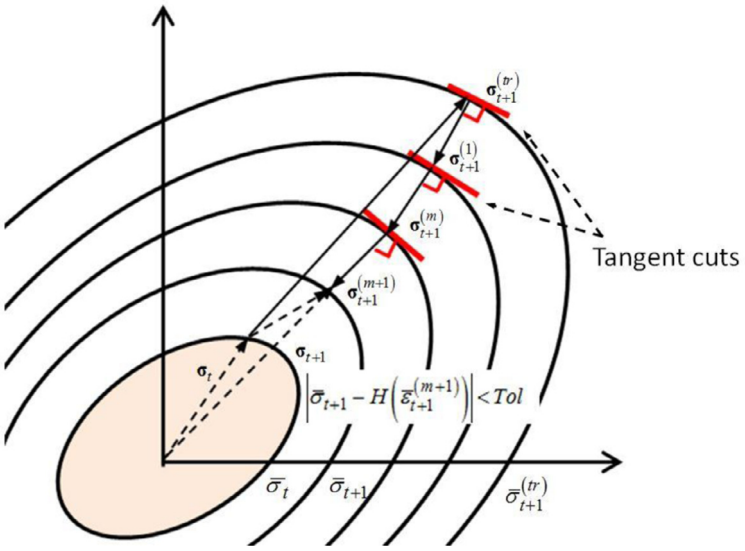

Fig. 1. Geometric interpretation showing the update stress scheme using the cutting plane algorithm in the stress space.

where the superscripts m and $m+1$ represent the previous and the current iteration steps, respectively. The variation of equivalent plastic strain (the last term in Eq. 23) for sub-iteration m can be obtained by Eq. (20) at iteration $m+1$ using

$$\delta(\Delta\bar{\varepsilon}_{t+1})^{(m+1)} = \frac{\Psi^{(m)}}{\left(\frac{\partial\bar{\sigma}_{t+1}}{\partial\boldsymbol{\sigma}_{t+1}}\mathbf{C}\frac{\partial\bar{\sigma}_{t+1}}{\partial\boldsymbol{\sigma}_{t+1}} + H'(\bar{\varepsilon}_{t+1})\right)^{(m)}} \tag{24}$$

Over the iteration process the stress, plastic strain, and other state variables $\Delta\hat{\mathbf{h}}^s$ (Eq. (3)) and $\Delta g_1 \rightarrow \Delta g_4$ (Eqs. (5) → (8)) which are related to the fluctuating component φ_h in Eq. (1) are updated as a function of $\delta(\Delta\bar{\varepsilon}_{t+1})^{(m+1)}$ at every iteration step, (see Appendix A). The iterative scheme carries forward until the prescribed numerical tolerance *Tol* satisfies the consistency condition $\Psi^{(m+1)} < Tol$ given below

$$\Psi\left(\boldsymbol{\sigma}_{t+1}^{(m+1)}\right) = \left[\varphi^q\left(\boldsymbol{\sigma}_{t+1}^{(m+1)}\right) + \varphi_h^q\left(\boldsymbol{\sigma}_{t+1}^{(m+1)}\right)\right]^{\frac{1}{q}} - H\left(\bar{\varepsilon}_{t+1}^{(m+1)}\right) < Tol \tag{25}$$

The geometric interpretation of the stress integration scheme (GCPM) is illustrated in Fig. 1. The subsequent iteration of each step is initiated by cutting a tangent plane on which the new variables are projected to the yield surface (Lee et al., 2012). The 1st stress estimate $\boldsymbol{\sigma}_{t+1}^{(1)}$ is determined from the normal cut to the tangent plane of the trial stress $\boldsymbol{\sigma}_{t+1}^{(tr)}$. Similarly the stress for the new $(m+1)$th is estimated from the previous iteration (m)th as depicted in Fig. 1. Since the HAH model introduces a continuous distortion to the yield surface, the gradient of yield function $\partial\bar{\sigma}(\boldsymbol{\sigma}_{t+1})/\partial\boldsymbol{\sigma}_{t+1}$ in Eq. (24) should be carefully computed and needs to account for the microstructure deviator, the loading direction and the evolution of plastic parameters. This is achieved by using the multi-step Newton-Raphson method proposed by (Lee et al., 2012).

3. Experimental procedures

The main purpose of the experimental part is to determine the initial yield locus of Ti-6Al-4 V. Based on the experimental measurements the yield function of the material is evaluated based on the Hill's 48 quadratic and the non-quadratic YLD2000-2D yield functions. Generally the standard uniaxial tensile test is employed to determine the material parameters for both yield function and hardening model. However, to improve model accuracy additional test methods have also been applied. Those include the in–plane biaxial tensile tests using cruciform specimens (Kuwabara et al., 1998) to determine biaxial yield strength σ_b and the anisotropy coefficient r_b required for the YLD2000-2D yield criterion. Additionally to that the plane strain tensile test (Flores et al., 2010) is often used to calibrate and quantify the yield function for the plane stress condition. Therefore in the following sections the important mechanical tests for characterization the quasi-static mechanical response of Ti64 alloy sheet at room temperature will be presented.

3.1. Experimental characterization

3.1.1. The as received material

The material is mill annealed cold rolled sheet of Ti-6Al-4 V with an average thickness of 1.17 mm. The microstructure majorly consists of α- phase with only small fractions of β-phase (Badr et al., 2015).The nominal chemical composition determined by Optical Emission Spectrometry (OES) is given in Table 1.

3.1.2. Anisotropy in tension

Quasi-static tensile tests were performed at room temperature with a 500 kN universal testing machine at a constant strain rate of $10^{-3}\ s^{-1}$ as advised in (Thomas Jr, 1979). In order to measure material anisotropy specimens oriented 0°, 15°, 30°,45°,60°,75° and 90° to the Rolling Direction (RD) were prepared following the ASTM E8 standard (Standard, 2008) and tested applying a constant strain rate of $10^{-3}\ s^{-1}$ for the entire duration of the test.

Longitudinal and transversal strains were measured using two independent extensometers installed along the axial and the width direction of the tensile specimen as shown in Fig. 2. Triplicate tests were performed and the results averaged. For each test the true stress σ, true longitudinal strain ε_l and the true strain in the width direction ε_w were determined using (Hu et al., 2002)

$$\sigma = S(1+e_l); \quad \varepsilon_l = ln(1+e_l); \quad \varepsilon_w = ln(1+e_w) \tag{26}$$

where S, e_l and e_w are the corresponding engineering values of stress and strain in longitudinal and width direction, respectively. The true plastic strains were subsequently determined from the total strains by subtracting the elastic strains using (Lademo et al., 1999)

$$\varepsilon_l^p = \varepsilon_l - \frac{\sigma}{E}; \quad \varepsilon_w^p = \varepsilon_w - \nu\frac{\sigma}{E} \tag{27}$$

where the superscript p denotes to the plastic strain, and the Poisson's ratio ν and Young's modulus E were calculated from the lin-

Table 1
Chemical composition of the Ti-6Al-4V.

	C	Si	Mn	Fe	Nb	Al	V	O	N	H	Ti
%Wt.	0.034	0.012	0.002	0.0391	0.033	6.09	4.18	0.022	0.019	0.0022	89.56

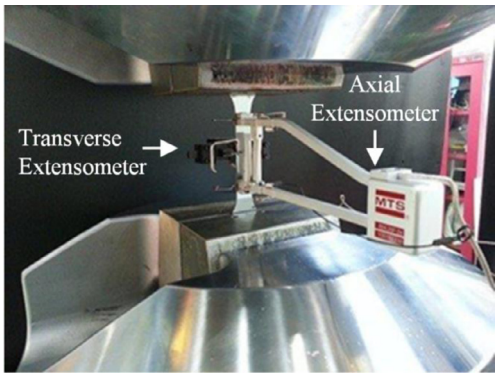

Fig. 2. Uniaxial tensile test applying longitudinal and transverse extensometers.

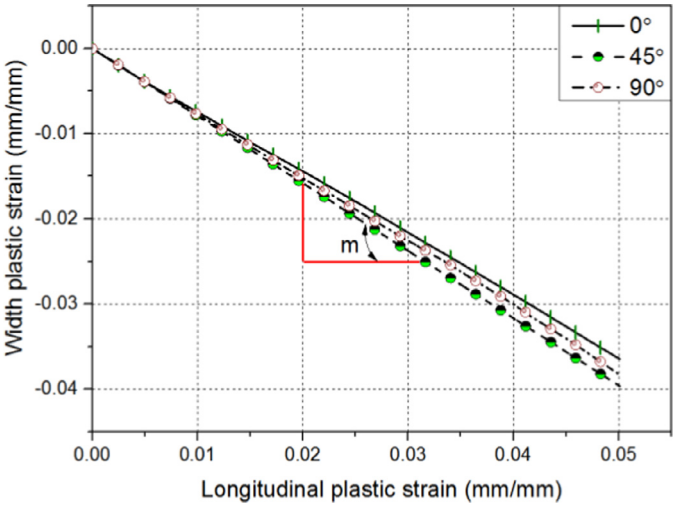

Fig. 3. Experimental measurements of transverse to longitudinal true plastic strain.

ear regression slope of the $\varepsilon_w - \varepsilon_l$ and $\sigma - \varepsilon$, respectively within the elastic part of the corresponding true stress strain curves. Based on Eq. (27) the ε_w can be calculated for each direction and plotted as a function of the ε_l as it is shown in Fig. 3 for sample orientations 0°,45° and 90°. The Lankford coeffecient r_θ (also called *r*-value or plastic strain ratio) is defined as the ratio of plastic strain in transverse to thickness directions. However, owing to the uncertainty associated with the direct measurement of the thickness strain ε_t this value was calculated based on the assumption of volume constancy during plastic deformation. All *r*-values were determined over a range of ε_l^p : $0 \leq \varepsilon_l^p \geq 0.05$ where elongation is uniform and the true transverse and longitudinal plastic strains can be assumed linearly proportional. As it can be observed by the linear regression slopes shown in Fig. 3 in the chosen measurement range, the *r*-values were found to be constant for all orientations. From the gradient of the linear regression *m* of the plot $\varepsilon_w^p - \varepsilon_l^p$ shown in Fig. 3, the *r*-value is calculated with

$$r_\theta = \left.\frac{\varepsilon_w^p}{\varepsilon_t^p}\right|_\theta = \left.\frac{-\varepsilon_w^p}{\left(\varepsilon_l^p + \varepsilon_w^p\right)}\right|_\theta = \left.\frac{-m}{1+m}\right|_\theta \tag{28}$$

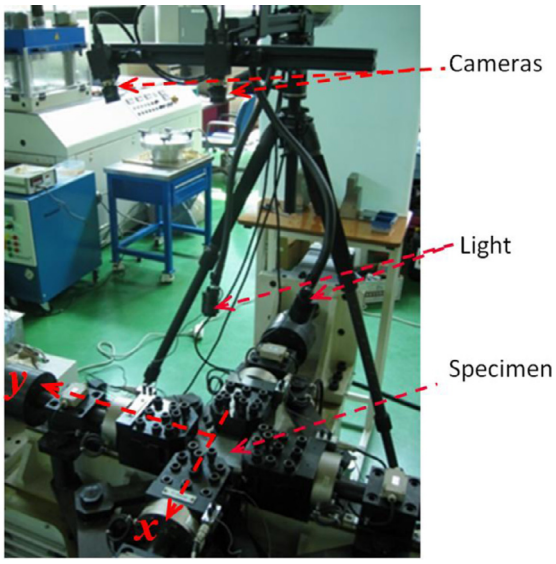

Fig. 4. In plane biaxial tensile test setup with the DIC.

3.1.3. In-plane biaxial test using cruciform specimens

To determine the initial yield surface in the positive quadrant in plane – biaxial tension tests were conducted using cruciform shaped specimens as proposed in (Kuwabara et al., 1998, Kuwabara et al., 2000, Hakoyama and Kuwabara, 2012). The testing machine is equipped with two pairs of cylinders aligned in the *x* and *y* directions. Details of the in-plane biaxial tensile machine and the set-up used in this study are shown in Fig. 4. The tensile forces F_x and F_y are measured by a load cell placed in each arm and were regulated to achieve specific load ratios for F_x: F_y using servo-controlled actuators. The tests were performed with three load ratios, 2:1, 1:1 and 1:2 at a strain rate of approximately $10^{-3}\ s^{-1}$ by controlling the crosshead speed of the actuators. Three repetitions for each load ratio were performed. The geometrical shape and dimensions of the cruciform specimen used in this study are shown in Fig. 5 as proposed by Kuwabara et al. (2000). The specimens were cut and fabricated from the as received Ti64 sheet using laser machining. The specimen surface was spray- painted with a stochastic pattern of white and black speckles. For each test, the specimen was first aligned and then gripped in the centre of the apparatus with four chucks aligning the RD and the TD of the specimen with the *x* and *y* arms of the machine (Fig. 4). A Digital Image Correlation (DIC) technique was utilized to measure the true strain in the Area Of Interest AOI (i.e. gauge area). This system is well suitable for full field and non-contact measurement of 3D deformations (Sutton et al., 2009; Iadicola et al., 2014; Lecompte et al., 2007). The DIC is equipped with a light source and two synchronized digital cameras to record the full deformation process (Fig. 4). Based on image correlation the strain is computed by comparing images of the specimen in deformed states with that of the initial or reference state assuming the conservation of the volume.

The procedure chosen for determining the true stress and strain components was the same previously applied by Hanabusa et al. (2013) who used an optical 3D deformation system in combination with the biaxial tensile test. The true stress components σ_{xx} and σ_{yy} (Eq. (29)) were calculated from the recorded load values F_x and F_y

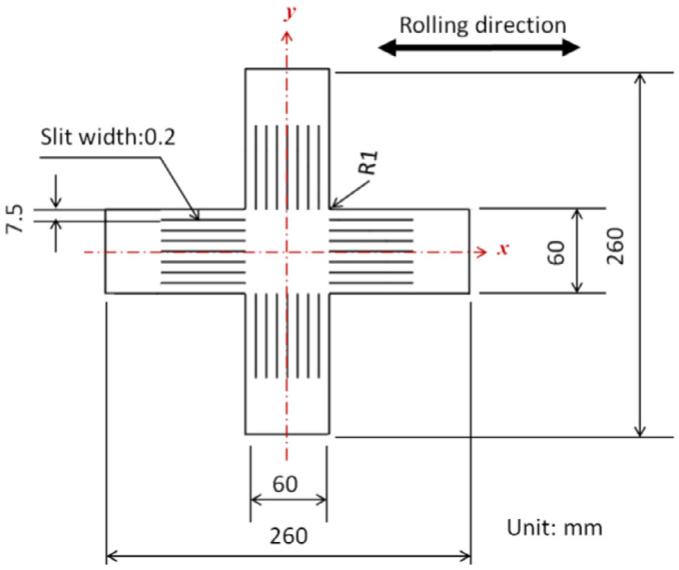

Fig. 5. Dimensions and shape of the cruciform specimen (Kuwabara et al., 2000).

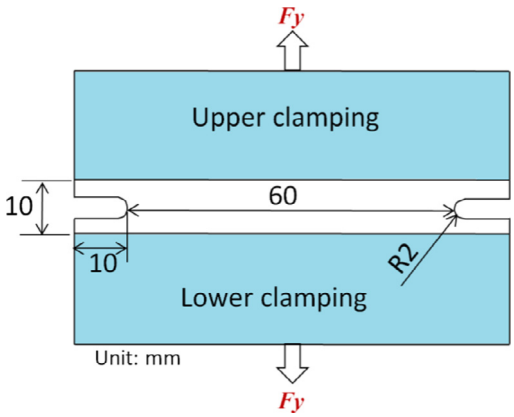

Fig. 6. Geometry of plane strain tensile specimen.

divided by the current cross- sectional area of the gauge section; this was determined from the measured values of the true strain components (ε_{xx} and ε_{yy}) applying the VIC-3D software package (VIC-3D user manual, 2005). In Eq. (29) volume constancy was assumed; the shear stress was assumed to be zero ($\sigma_{xy} = 0$) as the thickness strain observed by the VIC-3D was found to be nearly constant over the entire cross-sectional area in the middle of the specimen. The true strain components ε_{xx} and ε_{yy} were measured and averaged over the central section of 20 mm∗20 mm (AOI) of the entire gauge section (i.e. ε_i in Eq. (29)). From the stress- strain curves, obtained this way, for each load ratio and direction, the yield stress corresponding to the true plastic strain was determined with the offset line at $\varepsilon_i = 0.001$ parallel to the linear portion of the curves. For this the 0.1% offset strain method was applied instead of the commonly used 0.2% method. This was due to the lack of plastic deformation achievable before fracture occurred. The measured yield stresses were normalized to the tensile yield stress determined in rolling direction.

$$\sigma_i = (F/A_0).e^{(\varepsilon_i)} \tag{29}$$

where A_0 denotes the initial cross- sectional area of the AOI and i stands for the loading direction. The anisotropic biaxial coefficient r_b is defined as the slope of the linear fit to the true plastic strain ratio between the TD and the RD

$$r_b = \varepsilon^p_{yy}/\varepsilon^p_{xx} \tag{30}$$

3.1.4. Plane strain tensile test

The major advantage of the plane strain tension test (PSTT) is that it enables the experimental evaluation of the accuracy of the developed yield function with an ordinary tensile test set up. The geometrical drawing and dimensions of the specimen are shown in Fig. 6. Two in-plane loading directions RD and TD were analysed and three tests were performed for each orientation at a constant strain rate of 10^{-3} s^{-1}. Similar to the in-plane biaxial test in Section 3.1.3 the specimens were prepared with a speckle pattern and the true strain field over the specimen's surface was recorded using the DIC and then computed by the VIC-3D. The heterogeneous plane strain state resulting from the uniaxial stress states at the edges (Flores et al., 2010) was excluded from the measurement by only taking into account the central region (AOI) of the specimen as shown in Fig. 7. In this way, plane strain was only measured and averaged over a central gauge section having a width of 20 mm and a length of 20 mm (i.e. AOI). The true stress along the loading direction was then calculated on Eq. (29). The yield stress in the plane-strain tensile test was determined using the 0.2% offset strain method assuming volume constancy (Eq. (29)) and normalized to the tensile yield stress in RD. In Fig. 7 it can be observed that fracture did not occur in the gripping areas but occurred along the transvers centre of the specimen, which is an indication for a successful plane strain tension test.

3.1.5. Strength differential and Bauschinger effect

To characterize the material asymmetry in compression and tension as well as the Bauschinger behaviour upon reverse loading in-plane continuous tension-compression (T-C) and compression-tension (C-T) tests were conducted at room temperature. The experiments were performed using the experimental set up described by Kuwabara et al. (2009). In addition another set of experiments was carried out to characterize the forward-reverse loading behaviour of Ti64 over a single deformation cycle, which will be used later to examine the accuracy of the constitutive model developed in this study. Pin loaded samples were laser cut oriented in the RD and the TD. The geometry of the test specimen is shown in Fig. 8. Strain controlled tests were performed to a strain amplitude of ± 4.0% at a strain rate of 10^{-3} s^{-1} using a gauge section that was 25 mm wide and 50 mm long (Fig. 8). To prevent the occurrence of buckling in the axial direction during compressive loading, a stress normal to the sheet of 6.27 MPa was applied. The compressive force applied for this is a source of friction and biaxial stress and may result in the overestimation of the measured stress. The effect of the anti-buckling force therefore was excluded to compute the effective stress by calibration (Lee et al., 2005). For this purpose conventional tensile tests were performed with and without the applied clamping force on specimens oriented 0° and 90° to the rolling direction. Comparing both tests the correction factor was estimated to be 5.5%. Since the test in compression could not be performed without clamping force, the correction value determined in tension was applied to exclude the effect of friction and biaxial stress during compressive deformation. To quantify the Bauschinger effect the Bauschinger ratio β_e was calculated using (Lemoine and Aouafi, 2008)

$$\beta_e = \frac{\sigma_f - \sigma_r}{2\sigma_f} \tag{31}$$

Where σ_f denotes the flow stress where unloading starts and σ_r is the early re-yielding stress on reverse loading, defined by the 0.2% offset method with a slope equal to the original Young's modulus.

4. Experimental results and discussions

4.1. Results of quasi-static tension and anisotropic properties

The averaged true plastic stress–strain responses obtained from the quasi-static tension test are shown in Fig. 9 for the various

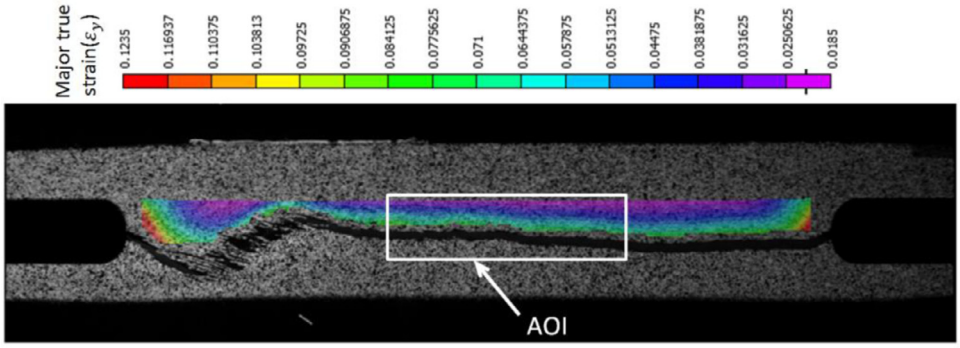

Fig. 7. Distribution of major true plane tensile strain at the fracture for specimen 90° with the AOI.

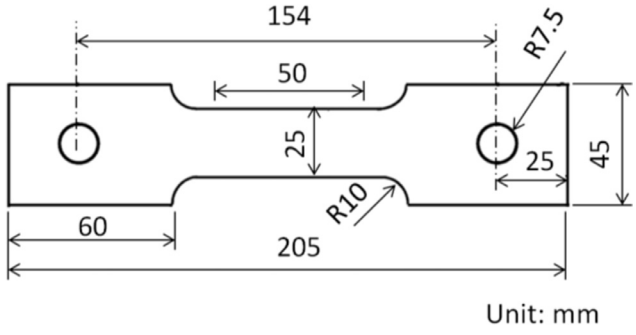

Fig. 8. Geometry of the in-plane tension compression specimen.

loading directions tested. It can be seen that the Ti64 exhibits a non-identical response in the mechanical properties, which is indicated by the difference in yield and flow stress as well as the total elongation (% El_{tot}.) determined for the various sample orientations. The 0.2% offset yield and the yield stress normalised in the rolling direction RD are shown for all sample directions in Table 2 together with *r*-values calculated using Eq. (28). These results are comparable with those previously reported for conventional Ti64 alloy sheet (Badr et al., 2015, Peters et al., 1984). The highest level of stress (i.e. yield strength and ultimate strength) was observed for samples oriented 90° to the RD, whereas samples oriented 45° to the RD showed the lowest material strength. This suggests the existence of orthotropy in the plane of Ti64 sheet, which is attributed to the HCP crystal structure and predominant crystallographic texture (Pederson, 2002). Tensile loading in the transverse direction parallel to the c-axis promotes the highest yield and ultimate tensile strengths, while the lowest stress values are generally observed when the orientation angle between the *c*-axis and the loading direction is 45° (Peters et al., 1984). The strong anisotropy is also indicated by the differences in the evolution of longitudinal versus transverse plastic strain shown in Fig. 3 between the different loading orientations. The maximum tensile stress is only

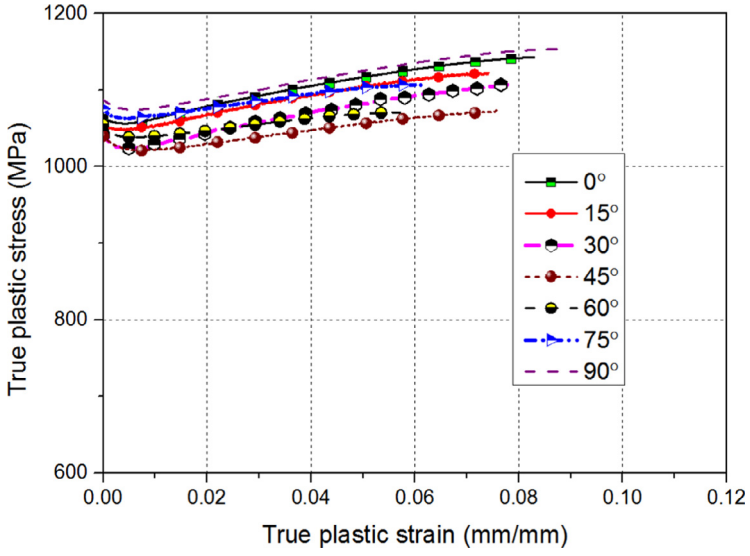

Fig. 9. True plastic stress- strain curves of Ti-6Al-4 V at different directions.

Table 2
In plane tensile yield stresses and strain anisotropy of Ti64 alloy sheet.

θ	0°	15°	30°	45°	60°	75°	90°
$\sigma_{0.2}[MPa]$	1064.0	1056.0	1041.0	1040.0	1055.0	1075.0	1087.0
$\sigma_\theta/\sigma_{0.2\,RD}$	1.0	0.992	0.978	0.9774	0.991	1.010	1.021
$\sigma_{U.T.S}[MPa]$	1143	1124	1109	1073	1070	1107	1156
% El_{tot}	12.49	11.6	12.57	13.40	10.55	10.0	12.9
r-value	2.57	2.82	3.34	3.80	3.74	3.16	3.10

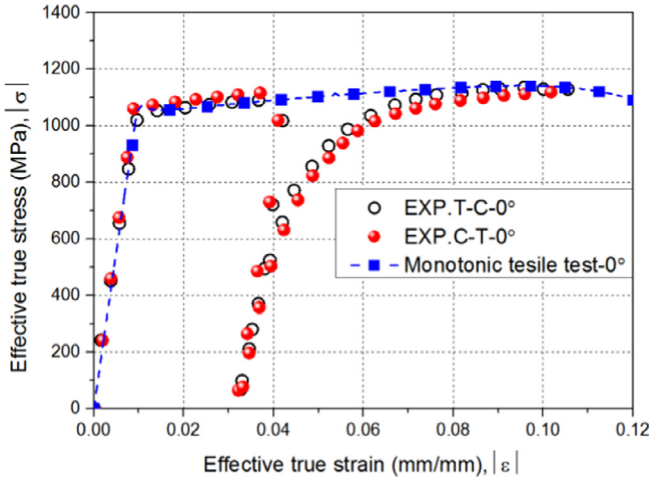

Fig. 10. Experimental results of compression/tension and tension/compression test compared to the monotonic tensile test for the RD.

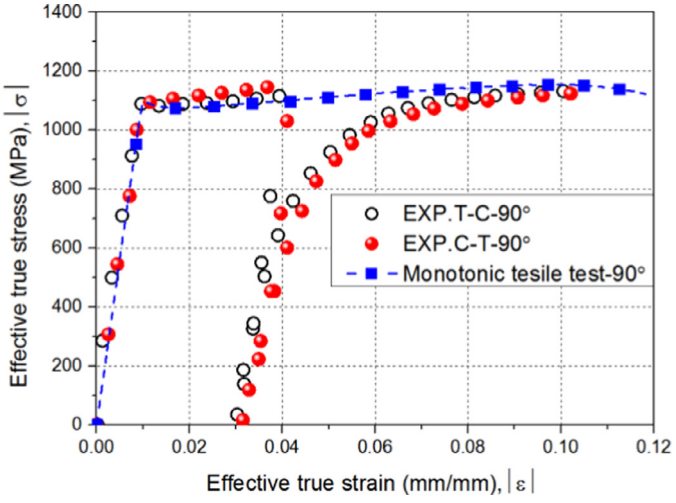

Fig. 11. Experimental results of compression/tension and tension/compression test compared to the monotonic tensile test for TD.

marginally higher than the yield stress for a given direction and this indicates the tendency for low strain hardening after yield (Table 2).

4.2. Asymmetry yielding and mechanical response on reverse loading

The average effective stress–strain response measured from the continuous T-C and C-T tests along the RD and the TD (after excluding the effect of the anti-buckling force) are compared to the monotonic tensile curves in Fig. 10 and Fig. 11, respectively. Here, the reverse flow curve of the T-C was moved to the tensile domain. The results of the C-T were drawn by translating the original plots by 180° with regard to the origin and moving the bottom half to the top quadrant, to allow the comparison with the T-C curve. It can be seen that the Ti64 exhibits an insignificant asymmetry between tension and compression at the onset of yielding in both the RD and the TD. The tension and compressive yield stresses (0.2% offset) were 1064 and 1080 [MPa], respectively for the RD and 1087 and 1105 [MPa] in TD. This corresponds to results reported for this alloy elsewhere (Gilles et al., 2011). However when the material is strained by compression first followed by tension the flow curve showed higher hardening compared to the curve involving tension followed by compressive deformation. This distortion in hardening evolution is more pronounced in the TD compared to RD. In accordance with the literature presented in (Lee et al., 2008) for most HCP- metals, the behaviour of Ti-6Al-4 V in yielding and flow stress can be considered as symmetric .The obtained material characteristics may indicate that the major deformation mode is slip based which agrees with previous study reporting that the amount of twinning dominated deformation in this particular alloy is below 1% at room temperature (Tirry et al., 2010). If the twinning deformation mode would have sufficiently developed during tension or compression at ± 0.04 strain, then a pronounced asymmetry would have been seen in the plastic behaviour between tension and compression as previously observed for CPTi (Nixon et al., 2010). This is because twinning is sensitive to one direction of loading while it is inactive in the opposite direction (i.e. directional dependence) (Cazacu et al., 2006). A possible reason for this observation is that, since the material is in a hard condition after rolling, the deformation microstructure is still well established. As a result, mechanisms such as twinning that were possibly active during the rolling process itself are, at this stage, exhausted. In addition, the high content of aluminium 6.09 wt. % and oxygen 0.022 wt% for the current Ti-6Al-4 V given in Table 1 retards the occurrence of twinning (Zaefferer, 2003, Conrad, 1981, Yapici et al., 2006). Therefore the distortional hardening in Ti64 observed in compression compared to tension may be due to the directionality of the dislocation structures and their arrangements (Kuwabara et al., 2009) and the strengthening of the texture evolution with increasing plastic deformation (Knezevic et al., 2013).

Table 3
The mechanical parameters of Ti64 alloy sheet obtained from; (a) the in plane biaxial cruciform tension test, (b) the plane strain tensile test PSTT.

(a) In plane biaxial cruciform test

σ_{xx}: σ_{yy}	σ_{xx}	σ_{yy}	σ_b	r_b
1:1	1.0244	1.0132	1.0188	1.289
2:1	1.0836	0.526	-	-
1:2	0.464	1.09	-	-

(b) Plane strain tensile test

$\sigma_{plane} - 0°$	1.12	0
$\sigma_{plane} - 90°$	0	1.15

Upon reverse deformation the Ti64 showed a pronounced propensity for early re-yielding i.e. Bauschinger effect followed by the transient behaviour characterized by a rapid change of the work hardening rate. The Bauschinger ratio β_e was empirically quantified using Eq. (31) from the T-C test at 4.0% pre-strain for both the RD and the TD and found to be 0.74 and 0.71, respectively. This means that the TD exhibits a slightly larger Bauschinger effect. No permanent softening was observed as indicated by the reverse flow curve fully recovering the stress levels of the forward flow curve (Figs. 10 and 11). With further loading and completion of the symmetric strain cycle at an amplitude of 4.0% as will be shown in Fig. 16 (a–d) in Section 6.1, the material cyclically hardened; the subsequent reloading curve is slightly higher than for the case of forward curve producing a permanent hardening offset. Although no studies with regard to the behaviour of Ti-6Al-4 V during reverse loading have been attempted yet, however the current results agree with the literature of high strength steels as the reverse deformation behaviour depends upon the pre-strain value. The offset stress between the flow curve during forward loading and the one upon reverse straining decreases when the pre-strain is large (Yoshida et al., 2002, Paul et al., 2011). Overall the results show that the Ti64 alloy investigated in this study shows tension - compression symmetry material with some asymmetry in hardening evolution.

5. Yield function of Ti-6Al-4 V at room temperature

Based on the experimental observations presented in Sections 4.1 and 4.2 two anisotropic yield functions, Hill's (1948) (see

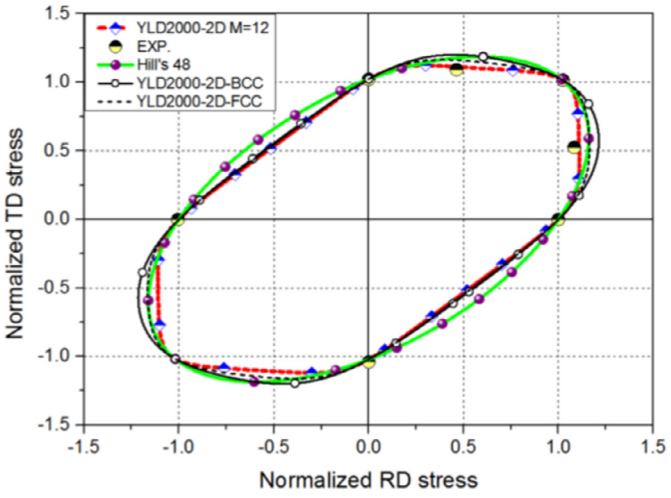

Fig. 12. Experimental yield points and predicted yield surfaces from two different yield criteria.

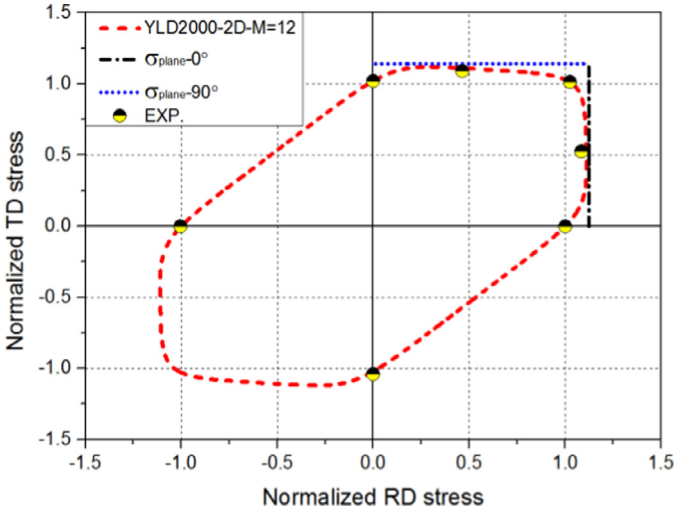

Fig. 13. Validation of adapted YLD2000-2D- $M = 12$ with experimental plane strain yield stresses in both the RD and the TD.

Appendix B) and YLD2000-2D (Barlat et al., 2003) (see Appendix C), were used to model the initial yield locus of the Ti64 alloy. The input parameters used for the Hill's quadratic yield criterion were $\sigma_0, \sigma_{45}, \sigma_{90}$ and r_0, while those for the non-quadratic YLD2000-2D were $\sigma_0, \sigma_{45}, \sigma_{90}, r_0, r_{45}$, and r_{90} with the biaxial coefficients $\sigma_b$and r_b determined in the equi-biaxial tension test and given in Table 3. The normalized yield stresses obtained from the cruciform test at different load ratios (Section 3.1.3) and the plane strain tensile tests (Section 3.1.4) are summarized in Table 3.

To model and calibrate the YLD2000-2D yield function the exponent M which is related to the crystal structure of the material was set at different values ($M = 6$ for BCC, $M = 8$ for FCC (Hosford, 1996, Logan and Hosford, 1980) and $M = 12$) and compared to experimentally measured data. Fig. 12 shows the comparison between the theoretical initial yield loci and the three stress states experimentally analysed in this study: uniaxial tension, in-plane biaxial tension and in-plane compression. The anisotropy coefficients of the quadratic and non-quadratic yield functions were calculated using a non-linear Newton–Raphson solver and are given in Table 4. It can be obviously seen in Fig. 12 that except for the plane strain condition the Hill's 48 as well as the Yld2000-2D for BCC and FCC yield surfaces give a good fit of the experimental yield stress values. The accuracy of the predicted yield locus is comparable to that achieved with the CPB06 yield function applied in (Gilles et al., 2011) and shows an elliptical shape. However comparison with the in-plane biaxial cruciform test results show that the plastic flow of Ti64 is overestimated in the directions between the biaxial stress point at $\sigma_{xx} : \sigma_{yy} = 1 : 1$ and the uniaxial stress conditions at $\sigma_{xx} : \sigma_{yy} = 1 : 0$ and at $\sigma_{xx} : \sigma_{yy} = 0 : 1$. To improve the accuracy of the YLD2000-2D yield function with experimental results for biaxial tension at the load ratios $\sigma_{xx} : \sigma_{yy} = 2 : 1$ and $\sigma_{xx} : \sigma_{yy} = 1 : 2$ the parameter M was varied using the values given above. The best fit of the yield surface description was found with $M = 12$ for all key stress states, as shown in Fig. 12. The accuracy of the defined yield surface can be further assessed to what extent it can reproduce the yielding behaviour of Ti-6Al-4 V obtained from different stress condition. For this, the normalized yield stresses determined in the plane strain tensile tests (Section 3.1.4) along the RD and the TD (Table 3 b) was added to the stress space (Fig. 13). It is obvious that both yield stresses; $\sigma_{plane} - 0^\circ$ and $\sigma_{plane} - 90^\circ$are almost tangent to the optimised YLD2000-2D yield description (Fig. 13). The YLD200-2D- $M = 12$ showed a good flexibility of closely reproducing the yielding behaviour under different stress states including loading ratio 2:1 and 1:2 as shown in (Fig. 12) as well as the plane strain yield stresses in both the RD and the TD (Fig. 13). This suggests that the YLD2000-2D ($M = 12$) represents the yield behaviour of Ti64 sufficiently and can reproduce its mechanical response under any stress conditions.

5.1. Application of the adapted YLD2000-2D

Now it is of great importance to further examine the capability of the optimized YLD2000-2D to describe the planar variations of tensile properties shown in Fig. 9 and listed in Table 2. Fig. 14 compares the normalized yield stress predicted by the calibrated YLD2000-2D and Hill's 48 yield function to the experimental results determined for samples oriented 0°, 15°, 30°, 45°, 60°, 75° and 90° from the RD. Additionally to that the experimental normalized plastic flow stresses determined at 0.02 and 0.04 plastic strains are compared to those theoretically predicted by the calibrated YLD2000-2D yield function. Fig. 15 compares the experimental anisotropy coefficients (r-values) with those predicted by the two yield criteria for the various sample orientations. It can be clearly seen that the adapted YLD2000-2D has the capability to represent the anisotropic hardening evolution and anisotropy coefficients of Ti64 up to a large level of plastic strain, whereas the Hill's 48 gives inaccurate results for the anisotropic parameters (r-values).This is due to that the Hill's 48 model is defined based on yield stress only instead of using strain approach (r-value). Based on that Hill's48 model is expected to predict the plastic flow stress at any plastic strain and therefore Hill's 48 yield function at

Table 4
Anisotropic parameters of Hill's 48 and YLD2000-2D for different values of M.

Hill48	F	G	H	N					
	0.416	0.463	0.537	1.654					
	M	A_1	A_2	A_3	A_4	A_5	A_6	A_7	A_8
YLD2000-2D	6	1.066	1.055	1.233	0.934	0.905	0.90	1.101	0.761
	8	1.064	1.02	1.136	0.948	0.933	0.965	1.086	0.838
	12	1.053	0.994	1.074	0.959	0.955	0.978	1.064	0.918

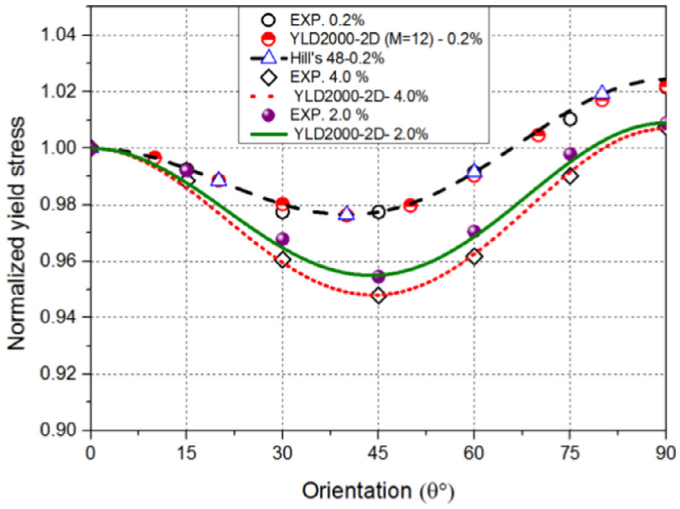

Fig. 14. The in plane normalized yield stress predicted by the YLD2000-2d ($M = 12$) and the Hill's 48 model, as well as the plastic flow stresses predicted by the YLD2000-2D ($M = 12$) at 0.002, 0.02 and 0.04 ε^p compared to experimental values.

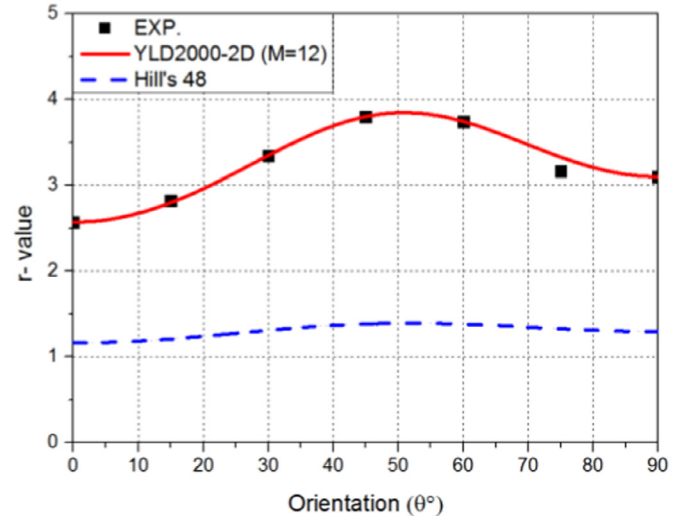

Fig. 15. In the plane Lankford coefficients predicted by the Hill's 48 and the YLD2000-2D ($M = 12$) yield criterion of the Ti-6Al-4 V sheet.

0.2% strain is used as an example to examine its accuracy as shown in Fig. 14. By applying the exponent $M = 12$ the YLD2000-2D yield criterion can accurately capture the deformation behaviour of Ti64 in sheet forming process at room temperature.

For determining the flow hardening of Ti64 in tension, it should be pointed out that either the concept of equal plastic strain and equal plastic work lead approximately to similar results. The determined flow stresses at $\varepsilon^p \cong 0.02$ and 0.04 correspond to those measured at equal plastic work $w^p \cong 21.3$ and 43.47 [MPa], respectively. This may be attributed to the gentle slope of the tensile flow curves of Ti64 observed for all orientations (Fig. 9) which indicates low work hardening.

6. FE – simulation of the cyclic stress–strain response of Ti64

The elastic–plastic model (HAH model) presented in Section 2.1 was introduced to reproduce the mechanical response of Ti64 during the continuous in plane T-C and C-T tests over a full cycle of symmetric strain of ± 4.0% in the RD and the TD. FE simulations of a single element were conducted using the implicit finite element code Abaqus / standard version 6.13 and the user material subroutine "UMAT" according the FE- formulation in Section 2.2. A reduced 4-node shell type (S4R) with 5 integration points through the thickness was used. Displacement boundary conditions were applied according to the experiments. The non-quadratic anisotropic yield function YLD2000-2D with the exponent $M = 12$ was considered as the associated stable component φ in the HAH formulation. Due to the negligible difference (≈2.5 %) determined for the Young's modulus E and the Poisson's ratio ν in the uniaxial tensile tests in RD and TD (Table 5) the effect of elastic anisotropy has been neglected. To determine the isotropic elastic constants, the values of the Young's modulus and the Poisson's ratio for the RD and TD were averaged. The anisotropic coefficients of $\varphi(A_1 \rightarrow A_8)$ provided in Table 4 were integrated into the constitutive model. The isotropic hardening parameters required for the condition of the flow rule Eq. (14) were determined by approximating the tensile flow curves along the RD and the TD using the Swift hardening law $\bar{\sigma} = H(\varepsilon_0 + \varepsilon^p)^n$. The resulting parameters are listed in Table 5. The material coefficients $k_1 \rightarrow k_5$ corresponding to the φ_h were then optimized while the coefficients of q in Eq.(1) and k in Eq. (3) were set equal to the values recommended by Barlat et al. (2011) since the data required for their calibration was not available. The evolutionary coefficients of HAH model are summarized in Table 6.

Table 5
Coefficients for hardening models of Ti64 at room temperature in 0° and 90°.

Property	Elasticity		IH		
	$G[GPa]$	ν	$H[MPa]$	ε_0	n
RD	116	0.36	1280	0.0114	0.047
TD	113	0.37	1325	0.0116	0.051

Table 6
Constitutive model parameters of HAH for Ti64 at room temperature in 0° and 90.

M	q	k	k_1	k_2	k_3	k_4	k_5
12	2	30	130	85	0.25	1.0	0.0

6.1. FE- simulation results and discussion

The stress–strain response over a full cycle of forward- reverse loading in the RD and the TD predicted by the proposed HAH model compared to the experimental results is shown in Fig. 16 (a–d) for a symmetric strain cycle of ± 4.0%. During load reversal the Bauschinger effect and the transient behaviour of Ti64 are accurately accounted for with the HAH model, Fig. 16 (a–d). The flow stress predicted by the HAH model saturates with similar intensity as the experimental measurements.

The current results can be explained based on the evolution of the yield surface of the HAH model. The evolution of the normalized yield locus under the HAH scheme for both the longitudinal and transverse directions in the π plane with the associated microstructure deviator $\hat{\mathbf{h}}$ and the stress states (i.e. $\mathbf{s}_t$ and $\mathbf{s}_c$ in tension and compression, respectively) are shown in Fig. 17a and b. These figures illustrate the changes in the initial state of the yield surface (dotted line) after 4.0% tension and after 4.0% subsequent compression upon reverse loading respectively compared to the evolution of the symmetric/isotropic yield surface (dotted line). In the case of load reversal the rotation of $\hat{\mathbf{h}}$ does not change. When the loading path changes from tension to the subsequent compression $\hat{\mathbf{h}}$ is aligned with the $\mathbf{s}_1$ (Fig. 17a) and $\mathbf{s}_2$ (Figs. 17b and 18) along the RD and TD, respectively. These results agree with those explained in detail by Barlat et al. (2011) and more detailed explanation can be found in (Barlat et al., 2011).

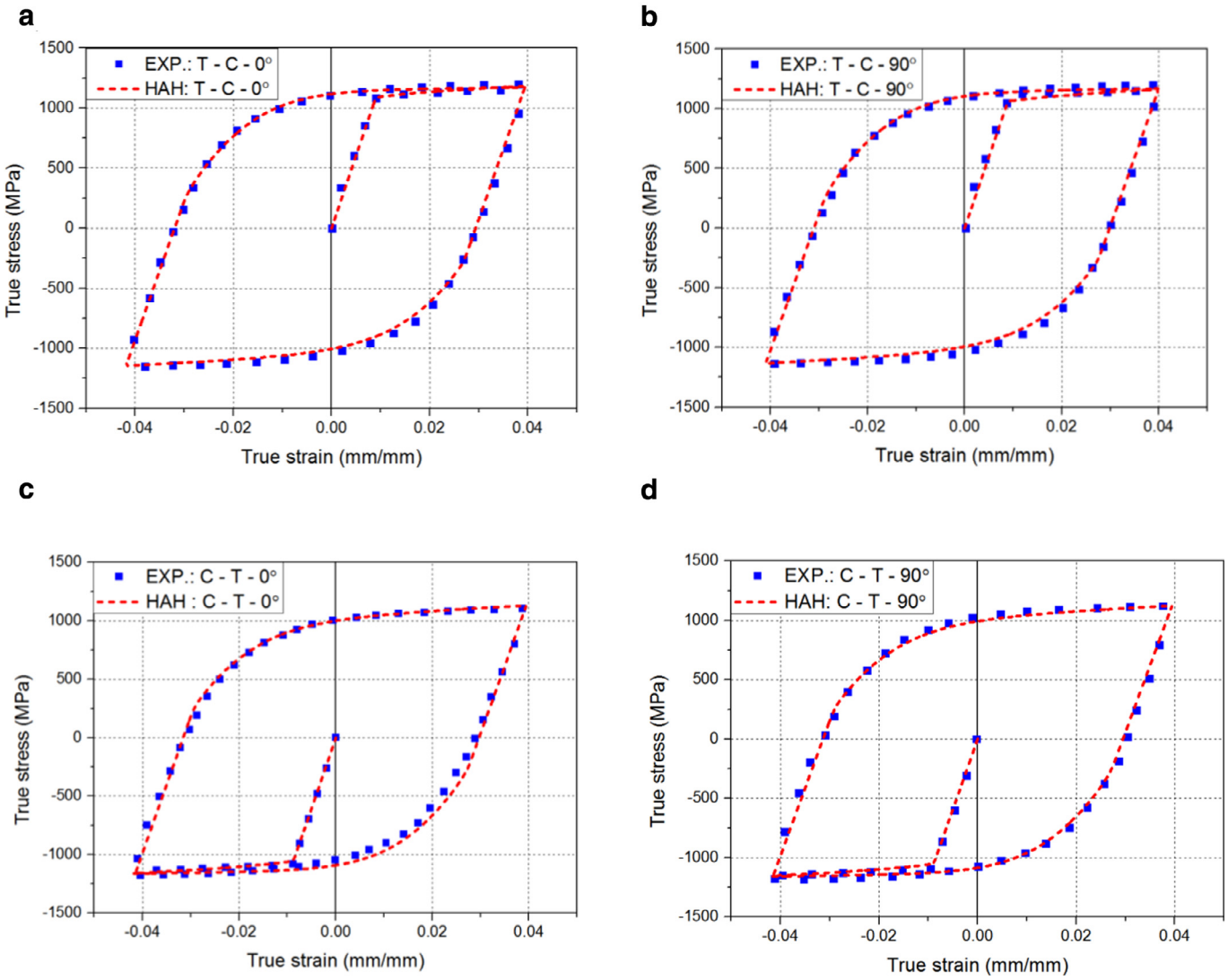

Fig. 16. (**a-d**) The predicted cyclic hardening T-C-T and C-T-C by HAH model in RD and TD at a strain amplitude of 4.0% in comparison with the experiments.

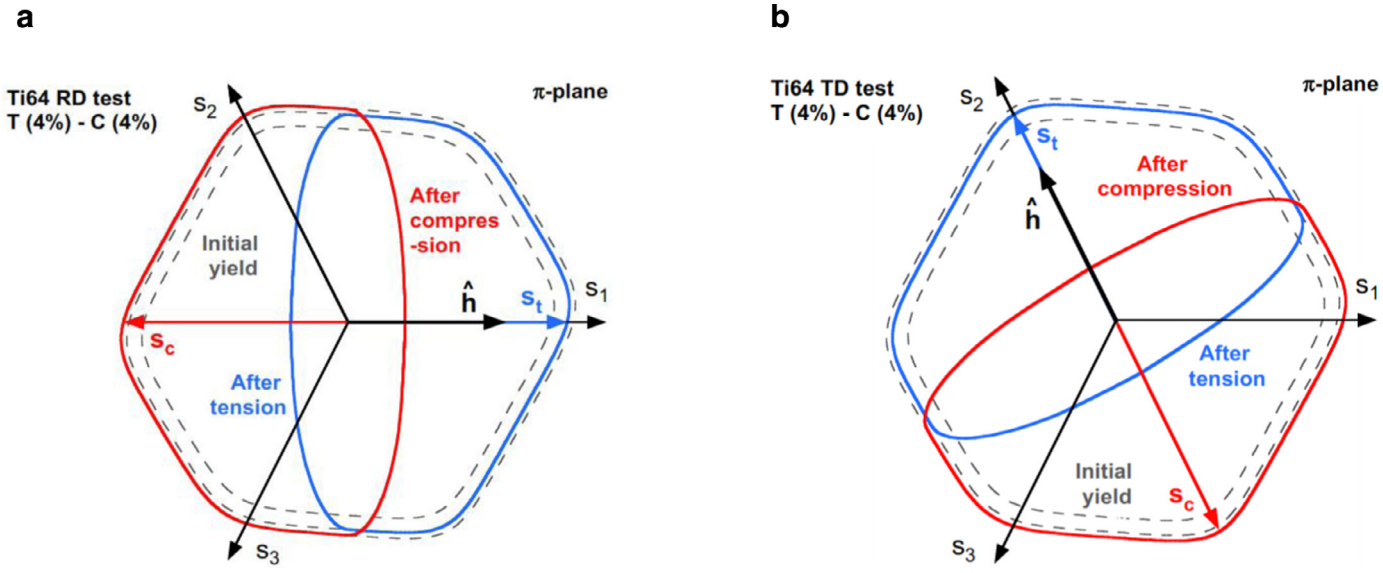

Fig. 17. Asymmetric yield loci for Ti-6Al-4 V in π plane after 4.0% tension and 4.0 % subsequent compression compared to the isotropic/symmetry state (dotted lines); a) RD, b) TD.

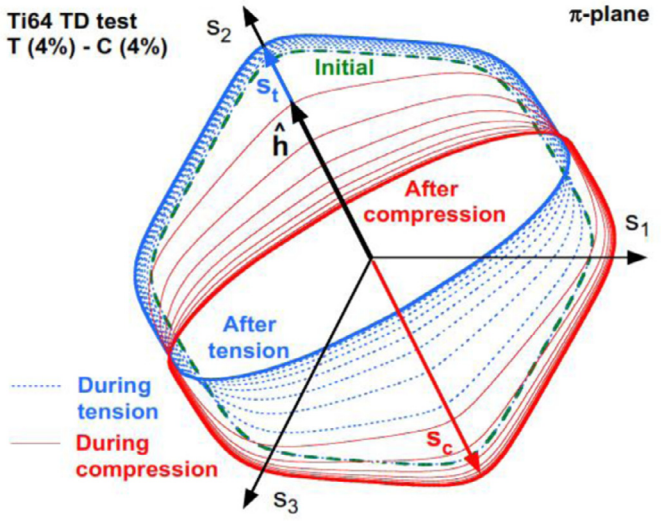

Fig. 18. Asymmetric yield loci for Ti-6Al-4 V in π plane after 4.0% tension and 4.0 % subsequent compression with evolution every 0.004 effective strain for TD loading under several reverse loadings.

During forward loading to 4.0% tension the side of the yield locus opposite to the direction of loading is flattened. When the load is subsequently reversed to 4.0% compression, the previously distorted side retrieves its original shape, while in the opposite direction the yield surface flattens (lower stress state) accounting for the Bauschinger effect. In addition to that, although the yield function (stable component) given in Eq. (1) is homogenous in stress, the formulation of the HAH is capable of producing a distortional yield surface associated to each particular direction with respect to the origin (Fig. 17 a and b). This allows it to describe the asymmetry in hardening of Ti-6Al-4 V, the Bauschinger effect and the transient behaviour for a continuous loading path and for multiple strain path changes.

For the case in which the yield locus varies under reverse loading according to the HAH model, Fig. 18 illustrates the distortional evolution of the yield surface, for instance in the transverse direction at several stages. It can be seen that the evolution patterns in both cases; only after tension and compression (Fig. 17 b), and during several reverse loadings (Fig. 18) are very similar.

It should be mentioned, here, that the Bauschinger effect and the transient behaviour under reverse loading can be affected by the strain amplitude. For now, only one strain amplitude of $\pm$ 0.04 was chosen to test the functionality of the model for predicting deformation behaviour at room temperature. Future research should include the application of the model to an actual forming case involving the fitting of various strain amplitudes.

7. Conclusions

A series of experiments and a theoretical investigation of the quasi-static plastic deformation behaviour of Ti64 alloy sheet were performed for different orientations at room temperature and low strain rate. The following conclusions can be made.

Quasi- static mechanical response of Ti64 alloy sheet

- Ti64 has strong material anisotropy. This is indicated by non-identical stress strain curves and differences in the Lankford values for different sample orientations.
- The direct comparison of the effective true stress strain curves determined in the tension and compression tests revealed that the strength differential effect between tension and compression is of insignificant value (SD < 2.0%) in both directions RD and TD, indicating the yielding behaviour is approximately symmetric. Whereas beyond the onset of yielding only small differences in the range of 1:1.05 in tensile to compressive hardening flow was observed for the TD and almost identical flow stresses for the RD.
- On reverse loading, a drop in the compressive flow stress was observed and quantified by Bauschinger ratio with 0.74 and 0.71 for 0° and 90°, respectively. The reduction in flow stress is followed by a rapid strain hardening. The material did not show any permanent softening, whereas with subsequent re-loading a slight cyclic hardening was observed.

Measured yield surface of Ti64

- The YLD2000-2D model calibrated with an exponent of $M = 12$ is able to accurately represent the yield surface and the in-plane sheet anisotropy of Ti64 at room temperature.

Elasto-plastic constitutive model

- Given that the measured asymmetry in yielding was quite insignificant. The anisotropic yield locus of Ti64 assumed symmetric, whereas the evolution of the anisotropic hardening assumed asymmetry.
- A constitutive model based HAH - model was then proposed and implemented into the FEA- Abaqus implicit solver using the material user subroutine UMAT. The FE- results of hardening cycle of Ti-6Al-4 V showed the novelty of the proposed constitutive model.
- The HAH model using the proposed hypothesis is capable of accurately describing the Bauschinger effect and the transient hardening behaviour of Ti64 during strain path reversal.

The proposed constitutive material model therefore presents a promising approach for the prediction of the material behaviour of Ti64 sheet in sheet metal forming processes at room temperature.

Acknowledgement

The authors appreciate the financial support of the Australian Research Council (ARC Linkage grant - LP120100111), and Australian Rollforming Manufacturers Pty Ltd. The authors would like to gratefully acknowledge the Materials Mechanics Laboratory team, GIFT-POSTECH for their support to conduct the experiments as well as the Korea Institute for Materials Science (KIMS).

Appendix A

The state variables of the fluctuating component in the yield function Eq. (1) and the plastic strain are updated during the iteration scheme until the condition $\Psi^{(m+1)} <$ Tol according to Eq. (25) is satisfied.

$$\delta(\Delta g_1)_{t+1}^{(m+1)} = \begin{Bmatrix} k_2\left(k_3 \frac{H(0)}{H(\bar{\varepsilon}_{t+1})} - (g_1)_{t+1}\right).\delta(\Delta\bar{\varepsilon}_{t+1})^{(m+1)} & \Rightarrow \hat{\boldsymbol{s}} : \hat{\mathbf{h}}^s \geq 0 \\ k_1 \frac{(g_4)_{t+1} - (g_1)_{t+1}}{(g_1)_{t+1}}.\delta(\Delta\bar{\varepsilon}_{t+1})^{(m+1)} & \Rightarrow \hat{\boldsymbol{s}} : \hat{\mathbf{h}}^s < 0 \end{Bmatrix} \quad \text{(A1)}$$

$$\delta(\Delta g_2)_{t+1}^{(m+1)} = \begin{Bmatrix} k_1 \frac{(g_3)_{t+1} - (g_2)_{t+1}}{g_2}.\delta(\Delta\bar{\varepsilon}_{t+1})^{(m+1)} & \Rightarrow \hat{\boldsymbol{s}} : \hat{\mathbf{h}}^s \geq 0 \\ k_2\left(k_3 \frac{H(0)}{H(\bar{\varepsilon}_{t+1})} - (g_2)_{t+1}\right).\delta(\Delta\bar{\varepsilon}_{t+1})^{(m+1)} & \Rightarrow \hat{\boldsymbol{s}} : \hat{\mathbf{h}}^s < 0 \end{Bmatrix} \quad \text{(A2)}$$

$$\delta(\Delta g_3)_{t+1}^{(m+1)} = \begin{Bmatrix} 0 & \Rightarrow \hat{\boldsymbol{s}} : \hat{\mathbf{h}}^s \geq 0 \\ k_5\left(k_4 - (g_3)_{t+1}\right).\delta(\Delta\bar{\varepsilon}_{t+1})^{(m+1)} & \Rightarrow \hat{\boldsymbol{s}} : \hat{\mathbf{h}}^s < 0 \end{Bmatrix} \quad \text{(A3)}$$

$$\delta(\Delta g_4)_{t+1}^{(m+1)} = \begin{cases} k_5\left(k_4 - (g_4)_{t+1}\right).\delta(\Delta\bar{\varepsilon}_{t+1})^{(m+1)} & \Rightarrow \hat{\boldsymbol{s}} : \hat{\mathbf{h}}^s \geq 0 \\ 0 & \Rightarrow \hat{\boldsymbol{s}} : \hat{\mathbf{h}}^s < 0 \end{cases} \tag{A4}$$

$$\delta(\Delta\hat{\mathbf{h}}^s)_{t+1}^{(m+1)} = \begin{cases} k\left[\hat{\boldsymbol{s}} - \frac{8}{3}\hat{\mathbf{h}}^s(\hat{\boldsymbol{s}} : \hat{\mathbf{h}}^s)\right]_{t+1}.\delta(\Delta\bar{\varepsilon}_{t+1})^{(m+1)} & \Rightarrow \hat{\boldsymbol{s}} : \hat{\mathbf{h}}^s \geq 0 \\ k\left[-\hat{\boldsymbol{s}} + \frac{8}{3}\hat{\mathbf{h}}^s(\hat{\boldsymbol{s}} : \hat{\mathbf{h}}^s)\right]_{t+1}.\delta(\Delta\bar{\varepsilon}_{t+1})^{(m+1)} & \Rightarrow \hat{\boldsymbol{s}} : \hat{\mathbf{h}}^s < 0 \end{cases} \tag{A5}$$

Therefore,

$$(\boldsymbol{\varepsilon}^p)_{t+1}^{(m+1)} = (\boldsymbol{\varepsilon}^p)_{t+1}^{(m)} + \delta\left[\Delta\bar{\varepsilon}_{t+1}\frac{\partial\bar{\sigma}\,(\boldsymbol{\sigma}_{t+1})^m}{\partial\boldsymbol{\sigma}_{t+1}}\right] \tag{A6}$$

$$(g_x)_{t+1}^{(m+1)} = (g_x)_{t+1}^{(m)} + \delta(\Delta g_x)_{t+1}^{(m+1)} \Rightarrow x = 1:4 \tag{A7}$$

$$(\hat{\mathbf{h}}^s)_{t+1}^{(m+1)} = (\hat{\mathbf{h}}^s)_{t+1}^{(m)} + \delta(\Delta\hat{\mathbf{h}}^s)_{t+1}^{(m+1)} \tag{A8}$$

Appendix B. Hill's yield function

For plane stress conditions and considering the axis of orthotropic anisotropy as the reference axes, Hill's 48 yield criterion can be reduced to a quadratic function (Hill, 1948) as follows:

$$\varphi\left(\sigma_{ij}\right) = \sigma^2{}_{xx}(G+H) - 2H\sigma_{xx}\sigma_{yy} + \sigma^2{}_{yy}(F+H) + 2N\sigma^2{}_{xy} = \bar{\sigma}^2 \tag{B1}$$

where σ_{xx}, σ_{yy} and σ_{xy} refer to the non-zero in- plane stress components.G, H, F and N are the material orthotropy coefficients that may be determined by following a stress based or strain (anisotropy coefficients) based approach.

Appendix C. YLD2000-2D yield function

Barlat et al. (2003) proposed a different non- quadratic yield function particularized for plane stress (2D), which can be expressed by:

$$\varphi = \left(\frac{\dot{\varphi} + \ddot{\varphi}}{2}\right)^{\frac{1}{M}} = \bar{\sigma} \tag{C1}$$

Where

$$\dot{\varphi} = \left|\dot{X}_1 - \dot{X}_2\right|^M \tag{C2}$$

$$\ddot{\varphi} = \left|2\ddot{X}_2 + \ddot{X}_1\right|^M + \left|2\ddot{X}_1 + \ddot{X}_2\right|^M \tag{C3}$$

Where the exponent M is related to the crystal structure of the material, M=6 is recommended for BCC and 8 for FCC (Hosford, 1996, Logan and Hosford, 1980). $\dot{X}_{12}$ and $\ddot{X}_{12}$ are the principal values of the stress tensors $\dot{\boldsymbol{X}}$ and $\ddot{\boldsymbol{X}}$, respectively**,** whose components can be obtained from performing two linear transformations on the Cauchy stress $\boldsymbol{\sigma}$ and the deviatoric Cauchy stress $\boldsymbol{S}$ tensors as follows:

$$\dot{\boldsymbol{X}} = \dot{\boldsymbol{C}}\boldsymbol{S} = \dot{\boldsymbol{C}}\boldsymbol{T}\boldsymbol{\sigma} = \dot{\boldsymbol{L}}\boldsymbol{\sigma} \tag{C4}$$

$$\ddot{\boldsymbol{X}} = \ddot{\boldsymbol{C}}\boldsymbol{S} = \ddot{\boldsymbol{C}}\boldsymbol{T}\boldsymbol{\sigma} = \ddot{\boldsymbol{L}}\boldsymbol{\sigma} \tag{C5}$$

Where the transformation matrix $\boldsymbol{T}$ (Eq. (C6)) transforms the Cauchy stress $\boldsymbol{\sigma}$ into its deviator, while other transformations $\dot{\boldsymbol{C}}$ and $\ddot{\boldsymbol{C}}$ are to introduce the anisotropy. The products of two transformations are represented as $\dot{\boldsymbol{L}}$ and $\ddot{\boldsymbol{L}}$ which can be given in form of matrix as below

$$\boldsymbol{T} = \begin{bmatrix} 2/3 & -1/3 & 0 \\ -1/3 & 2/3 & 0 \\ 0 & 0 & 1 \end{bmatrix} \tag{C6}$$

$$\begin{bmatrix} \dot{X}_{xx} \\ \dot{X}_{yy} \\ \dot{X}_{xy} \end{bmatrix} = \begin{bmatrix} \dot{L}_{11} & \dot{L}_{12} & 0 \\ \dot{L}_{21} & \dot{L}_{22} & 0 \\ 0 & 0 & \dot{L}_{66} \end{bmatrix} = \begin{bmatrix} \sigma_{xx} \\ \sigma_{yy} \\ \sigma_{xy} \end{bmatrix} \tag{C7}$$

$$\begin{bmatrix} \ddot{X}_{xx} \\ \ddot{X}_{yy} \\ \ddot{X}_{xy} \end{bmatrix} = \begin{bmatrix} \ddot{L}_{11} & \ddot{L}_{12} & 0 \\ \ddot{L}_{21} & \ddot{L}_{22} & 0 \\ 0 & 0 & \ddot{L}_{66} \end{bmatrix} = \begin{bmatrix} \sigma_{xx} \\ \sigma_{yy} \\ \sigma_{xy} \end{bmatrix} \tag{C8}$$

Where the coefficients of $\dot{\boldsymbol{L}}$ and $\ddot{\boldsymbol{L}}$ are expressed a**s:**

$$\begin{bmatrix} \dot{L}_{11} \\ \dot{L}_{12} \\ \dot{L}_{21} \\ \dot{L}_{22} \\ \dot{L}_{66} \end{bmatrix} = \begin{bmatrix} 2/3 & 0 & 0 \\ -1/3 & 0 & 0 \\ 0 & -1/3 & 0 \\ 0 & 2/3 & 0 \\ 0 & 0 & 1 \end{bmatrix} = \begin{bmatrix} A_1 \\ A_2 \\ A_7 \end{bmatrix} \tag{C9}$$

$$\begin{bmatrix} \ddot{L}_{11} \\ \ddot{L}_{12} \\ \ddot{L}_{21} \\ \ddot{L}_{22} \\ \ddot{L}_{66} \end{bmatrix} = 1/9\begin{bmatrix} -2 & 2 & 8 & -2 & 0 \\ 1 & -4 & -4 & 4 & 0 \\ 4 & -4 & -4 & 1 & 0 \\ -2 & 8 & 2 & -2 & 0 \\ 0 & 0 & 0 & 0 & 9 \end{bmatrix} = \begin{bmatrix} A_3 \\ A_4 \\ A_5 \\ A_6 \\ A_8 \end{bmatrix} \tag{C10}$$

Due to the fact that the linear transformations are incorporated with 8 anisotropy coefficients A_1–A_8 it is required to have 8 material characteristics for evaluating them. These coefficients can be determined from the uniaxial tensile test along rolling RD, diagonal 45° and transverse directions TD; three yield stresses and 3 coefficient of uniaxial anisotropy, together with balanced biaxial tension tests; biaxial yield stress σ_b and coefficient of biaxial anisotropy r_b.

References

Badr, O.M., et al., 2015. Forming of high strength titanium sheet at room temperature. Mater. Des. 66, 618–626.

Banabic, D., et al., 2010. Advances in anisotropy and formability. Int. J. Mater. Form. 3 (3), 165–189.

Banker, J.G., Scaturro, M., Feb., 1997. Titanium for secondary marine structures. In: Proceedings of International Workshop on Advanced Materials for Marine Construction.

Barlat, F., et al., 2003. Plane stress yield function for aluminum alloy sheets—part 1: theory. Int. J. Plast. 19 (9), 1297–1319.

Barlat, F., et al., 2011. An alternative to kinematic hardening in classical plasticity. Int. J. Plast. 27 (9), 1309–1327.

Cazacu, O., Plunkett, B., Barlat, F., 2006. Orthotropic yield criterion for hexagonal closed packed metals. Int. J. Plast. 22 (7), 1171–1194.

Chung, K., Richmond, O., 1993. A deformation theory of plasticity based on minimum work paths. Int. J. Plast. 9 (8), 907–920.

Chung, K., Shah, K., 1992. Finite element simulation of sheet metal forming for planar anisotropic metals. Int. J. Plast. 8 (4), 453–476.

Conrad, H., 1981. Effect of interstitial solutes on the strength and ductility of titanium. Prog. Mater. Sci. 26 (2–4), 123–403.

Djavanroodi, F., Derogar, A., 2010. Experimental and numerical evaluation of forming limit diagram for Ti6Al4V titanium and Al6061-T6 aluminum alloys sheets. Mater. Des. 31 (10), 4866–4875.

Donachie, M.J., 2000. Titanium: A Technical Guide. ASM International.

Flores, P., et al., 2010. Accurate stress computation in plane strain tensile tests for sheet metal using experimental data. J. Mater. Process. Technol. 210 (13), 1772–1779.

Gerd, Lütjering, J.C., Williams, 2007. Engineering Materials and Processes-Titanium, 2nd ed. Springer, Berlin.

Gilles, G., et al., 2011. Experimental characterization and elasto-plastic modeling of the quasi-static mechanical response of TA-6 V at room temperature. Int. J. Solids Struct. 48 (9), 1277–1289.

Gurrappa, I., 2003. Characterization of titanium alloy Ti-6Al-4 V for chemical, marine and industrial applications. Mater. Charact. 51 (2), 131–139.

Hakoyama, T., Kuwabara, T., 2012. Biaxial tensile test of high strength steel sheet for large plastic strain range. Key Eng. Mater. 504, 59–64.

Hanabusa, Y., Takizawa, H., Kuwabara, T., 2013. Numerical verification of a biaxial tensile test method using a cruciform specimen. J. Mater. Process. Technol. 213 (6), 961–970.

Hill, R. A Theory of the Yielding and Plastic Flow of Anisotropic Metals. 1948.

Hosford, W.F., 1996. On the crystallographic basis of yield criteria. Textures Microstruct. 27 (1), 479–494.

Hu, J., Marciniak, Z., Duncan, J., 2002. Mechanics of Sheet Metal Forming. Butterworth-Heinemann, pp. 6–9.

Iadicola, M.A., Creuziger, A.A., Foecke, T., 2014. Advanced biaxial cruciform testing at the NIST center for automotive lightweighting. Residual Stress, Thermomechanics & Infrared Imaging, Hybrid Techniques and Inverse Problems, 8. Springer, pp. 277–285.

Khan, A.S., Kazmi, R., Farrokh, B., 2007. Multiaxial and non-proportional loading responses, anisotropy and modeling of Ti–6Al–4 V titanium alloy over wide ranges of strain rates and temperatures. Int. J. Plast. 23 (6), 931–950.
Knezevic, M., et al., 2013. Modeling bending of α-titanium with embedded polycrystal plasticity in implicit finite elements. Mater. Sci. Eng. A 564 (0), 116–126.
Kuwabara, T., et al., 2000. Use of abrupt strain path change for determining subsequent yield surface: experimental study with metal sheets. Acta Materialia 48 (9), 2071–2079.
Kuwabara, T., et al., 2009. Tension-compression asymmetry of phosphor bronze for electronic parts and its effect on bending behavior. Int. J. Plast. 25 (9), 1759–1776.
Kuwabara, T., Ikeda, S., Kuroda, K., 1998. Measurement and analysis of differential work hardening in cold-rolled steel sheet under biaxial tension. J. Mater. Process. Technol. 80, 517–523.
Lademo, O.G., Hopperstad, O.S., Langseth, M., 1999. Evaluation of yield criteria and flow rules for aluminum alloys. Int. J. Plast. 15 (2), 191–208.
Lecompte, D., et al., 2007. Mixed numerical–experimental technique for orthotropic parameter identification using biaxial tensile tests on cruciform specimens. Int. J. Solids Struct. 44 (5), 1643–1656.
Lee, J.-W., Lee, M.-G., Barlat, F., 2012. Finite element modeling using homogeneous anisotropic hardening and application to spring-back prediction. Int. J. Plast. 29 (0), 13–41.
Lee, J.-Y., et al., 2012. An application of homogeneous anisotropic hardening to spring-back prediction in pre-strained U-draw/bending. Int. J. Solids Struct. 49 (25), 3562–3572.
Lee, M.G., et al., 2005. Spring-back evaluation of automotive sheets based on isotropic-kinematic hardening laws and non-quadratic anisotropic yield functions: Part II: Characterization of material properties. Int. J. Plast. 21 (5), 883–914.
Lee, M.-G., et al., 2008. Constitutive modeling for anisotropic/asymmetric hardening behavior of magnesium alloy sheets. Int. J. Plast. 24 (4), 545–582.
Lemoine, X., Aouafi, A., 2008. Bauschinger effect correspondence of experimental tests. Int. J. Mater. Form. 1 (1), 241–244.
Logan, R.W., Hosford, W.F., 1980. Upper-bound anisotropic yield locus calculations assuming $<$ 111$>$-pencil glide. Int. J. Mech. Sci. 22 (7), 419–430.
Lowden, M.A.W., Hutchinson, W.B., 1975. Texture strengthening and strength differential in titanium-6Al-4 V. Metall. Trans. A 6 (3), 441–448.
Moiseyev, V.N., 2005. Titanium Alloys: Russian Aircraft And Aerospace Applications. CRC Press.
Nixon, M.E., Cazacu, O., Lebensohn, R.A., 2010. Anisotropic response of high-purity α-titanium: experimental characterization and constitutive modeling. Int. J. Plast. 26 (4), 516–532.
Paul, S.K., et al., 2011. Cyclic plastic deformation behavior in SA333 Gr. 6 C–Mn steel. Mater. Sci. Eng. A 528 (24), 7341–7349.
Pederson, R., 2002. Microstructure and phase transformation of Ti-6Al-4 V. Applied Physics and Mechanical Engineering / Engineering Materials. Lulea University of Technology.
Peters, M., et al., 2003. Titanium alloys for aerospace applications. Adv. Eng. Mater. 5 (6), 419–427.
Peters, M., Gysler, A., Ütjering, G.L., 1984. Influence of texture on fatigue properties of Ti-6Al-4 V. Metall. Trans. A 15 (8), 1597–1605.
Plunkett, B., et al., 2006. Anisotropic yield function of hexagonal materials taking into account texture development and anisotropic hardening. Acta Materialia 54 (16), 4159–4169.
Plunkett, B., Cazacu, O., Barlat, F., 2008. Orthotropic yield criteria for description of the anisotropy in tension and compression of sheet metals. Inter. J. Plast. 24 (5), 847–866.
Prakash, D.L., et al., 2010. Deformation twinning in Ti-6Al-4 V during low strain rate deformation to moderate strains at room temperature. Mater. Sci. Eng. A 527 (21), 5734–5744.
Salem, A.A., Kalidindi, S.R., Doherty, R.D., 2003. Strain hardening of titanium: role of deformation twinning. Acta Materialia 51 (14), 4225–4237.
Schauerte, O., Ag, V., 2005. Titanium In Automotive Production. Wiley, Wolfsburg, Germany.
Simof, J. and T. Hughes, Computational Inelasticity. 2008.
Standard, A., 2008. E8/E8M: Standard Test Methods for Tension Testing of Metallic Materials. American Society for Testing Materials, Annual Book of ASTM Standards, Philadelphia, USA.
Sutton, M.A., Orteu, J.-J., Schreier, H.W., 2009. Image Correlation For Shape, Motion And Deformation Measurements, 10. Springer, New York pp. 978–970.
Thomas Jr, J.F., Determination Of Constitutive Equations For High Strength Aluminum And Titanium Alloys Applicable To Sheet Metal Formability. 1979, DTIC Document.
Tirry, W., et al., 2010. A multi-scale characterization of deformation twins in Ti6Al4V sheet material deformed by simple shear. Mater. Sci. Eng. A 527 (16–17), 4136–4145.
Welsh, G., Boyer, R., Collings, E., 1994. Materials Properties Handbook: Titanium Alloys. ASM International, Materials Park, OH.
VIC-3D User Manual. Correlated Solutions, Columbia, SC, 2005. http://www.correlatedsolutions.com/vic-3d/ (accessed 15.03.14).
Yapici, G.G., Karaman, I., Luo, Z.-P., 2006. Mechanical twinning and texture evolution in severely deformed Ti–6Al–4 V at high temperatures. Acta Materialia 54 (14), 3755–3771.
Yoshida, F., Uemori, T., Fujiwara, K., 2002. Elastic-plastic behavior of steel sheets under in-plane cyclic tension-compression at large strain. Int. J. Plast. 18 (5–6), 633–659.
Zaefferer, S., 2003. A study of active deformation systems in titanium alloys: dependence on alloy composition and correlation with deformation texture. Mater. Sci. Eng. A 344 (1–2), 20–30.